

REPORT DOCUMENTATION PAGE			Form Approved OMB NO. 0704-0188	
Public Reporting burden for this collection of information is estimated to average 1 hour per response, including the time for reviewing instructions, searching existing data sources, gathering and maintaining the data needed, and completing and reviewing the collection of information. Send comment regarding this burden estimates or any other aspect of this collection of information, including suggestions for reducing this burden, to Washington Headquarters Services, Directorate for information Operations and Reports, 1215 Jefferson Davis Highway, Suite 1204, Arlington, VA 22202-4302, and to the Office of Management and Budget, Paperwork Reduction Project (0704-0188,) Washington, DC 20503.				
1. AGENCY USE ONLY (Leave Blank)		2. REPORT DATE October 15, 2006		3. REPORT TYPE AND DATES COVERED Final Progress Report May 15, 2001 - October 14, 2006
4. TITLE AND SUBTITLE Fundamental Research on Infrared Detection			5. FUNDING NUMBERS DAAD19-01-1-0591 ARO Proposal no. 42210-EL-MUR	
6. AUTHOR(S) S. L. Chuang, Y. C. Chang, K. Y. Cheng, R. D. Dupuis, K. C. Hsieh, and J. O. White				
7. PERFORMING ORGANIZATION NAME(S) AND ADDRESS(ES) University of Illinois at Urbana-Champaign, 1406 W. Green St., Urbana, IL 61801			8. PERFORMING ORGANIZATION REPORT NUMBER MURI-UIUC-GIT-05	
9. SPONSORING / MONITORING AGENCY NAME(S) AND ADDRESS(ES) U. S. Army Research Office (Attn: Dr. William Clark) P.O. Box 12211 Research Triangle Park, NC 27709-2211			10. SPONSORING / MONITORING AGENCY REPORT NUMBER	
11. SUPPLEMENTARY NOTES The views, opinions and/or findings contained in this report are those of the author(s) and should not be construed as an official Department of the Army position, policy or decision, unless so designated by other documentation.				
12 a. DISTRIBUTION / AVAILABILITY STATEMENT Approved for public release; distribution unlimited.			12 b. DISTRIBUTION CODE	
13. ABSTRACT (Maximum 200 words) Fundamental research issues on infrared photodetectors are reported. These include the following: Task 1. HgCdTe (MCT) defect study – Continuing the research on degradation of MCT, we explore the size changing of the dislocation loops and the effect of low-dose electron beam irradiation during TEM analysis. Self-energy correction is included to calculate the MCT defect states. For the photoluminescence image, we correlate the PL images from MCTs and their CZT substrates. Task 2. Antimony-based type-II superlattice (T2-SL) photodetectors – We explored the temperature dependent and noise current characteristics of interband cascade detectors (ICDs). We also acquired type-II superlattice photodiodes from Jet Propulsion Lab and obtained a high detectivity of 5.23×10^{10} cmHz ^{1/2} /W at 77 K with devices of 10.5 μm cutoff wavelength. Moreover, MOCVD growth of InAs/GaSb type-II superlattices was explored with substrates of both GaSb and GaAs. Task 3. Quantum dot infrared photodetectors (QDIPs) – Our work has been focused on the growth and fabrication of high performance QDIP devices based on technologies developed. Defect-free 100-period InAs QD structure has been demonstrated. For InAs QDIPs grown on InP substrates by molecular beam epitaxy (MBE), peak detectivity of 2.1×10^9 cmHz ^{1/2} /W was achieved at a bias voltage of 0.8V.				
14. SUBJECT TERMS Infrared photodetectors, mercury-cadmium telluride (MCT) photodetectors, antimony Type-II superlattice, quantum-dot infrared photodetectors, defects, transmission electron microscopy			15. NUMBER OF PAGES 32	
			16. PRICE CODE	
17. SECURITY CLASSIFICATION OR REPORT UNCLASSIFIED	18. SECURITY CLASSIFICATION ON THIS PAGE UNCLASSIFIED	19. SECURITY CLASSIFICATION OF ABSTRACT UNCLASSIFIED	20. LIMITATION OF ABSTRACT UL	

REPORT DOCUMENTATION PAGE (SF298)
(Continuation Sheet)

1. List of papers submitted or published under ARO sponsorship during this reporting period

(a) Manuscripts submitted, but not published:

R. Furstenberg, J.O. White, J.H. Dinan, "Photoluminescence study of the 1.3-1.55 eV defect band in CdTe and $\text{Cd}_{0.96}\text{Zn}_{0.04}\text{Te}$," submitted to Journal of Applied Physics.

R. Furstenberg and J. O. White, "Correction of the Distortion of Luminescence Spectra in Multilayered Structures" submitted to Journal of Luminescence.

R. Furstenberg and J.O. White, "Error-free phase correction of interferograms using digital all-pass filters," to be published in Vibrational Spectroscopy.

X. B. Zhang, J. H. Ryou, R. D. Dupuis, A. Petschke, S. Mou, S. -L. Chuang, C. Xu, and K. -C. Hsieh, "Improved surface and structural properties of InAs/GaSb superlattices on (001) GaSb substrate by introducing an InAsSb layer at interfaces, Appl. Phys. Lett. (submitted for publication).

(b) Papers published in peer-review journals:

J. Kim, M. Lerttamrab, S. L. Chuang, C. Gmachl, D. L. Sivco, F. Capasso, and A. Y. Cho, "Theoretical and experimental study of optical gain and linewidth enhancement factor of type-I quantum cascade lasers," *IEEE J. Quantum Electron.*, **40**, 1663 (2004)

J. V. Li, O. V. Sulima, J. A. Cox, and S. L. Chuang, "Passivation of AlGaAsSb/InGaAsSb/GaSb photodiodes using aqueous $(\text{NH}_4)_2\text{S}$ solution and polyimide encapsulation," *J. Appl. Phys.*, **97**, 104506 (2005).

J. V. Li, S. L. Chuang, and R. Q. Yang, "Room temperature mid-infrared photovoltaic detectors based on type-II interband cascade structure," *Appl. Phys. Lett.*, **86**, 101102 (2005).

J. V. Li, S. L. Chuang, E. M. Jackson, E. Aifer, "Minority carrier diffusion length and lifetime for electrons in a type-II InAs/GaSb superlattice photodiode," *Appl. Phys. Lett.*, **85**, 1984 (2004).

J. Velev and Y. C. Chang, "Finite size effects on the conductance and giant magnetoresistance of Fe/Cr and Co/Cu nanowires," *Phys. Rev. B* **67**, 144425, (2003).

M. Lerttamrab, S. L. Chuang, R. Q. Yang, and C. J. Hill, "Linewidth enhancement factor of a type-II interband-cascade laser," *J. Appl. Phys.* **96**, 3568 (2004).

M. Lerttamrab, S. L. Chuang, C. Gmachl, D. L. Sivco, F. Capasso, and A. Y. Cho, "Linewidth enhancement factor of a type-I quantum-cascade laser," *J. Appl. Phys.*, vol. 94, pp. 5426-5428, (2003).

R. Furstenberg, J.A. Soares, and J.O. White, "Apparatus for the imaging of infrared photoluminescence, transmittance, and phototransmittance with high spatial and spectral resolution," *Review of Scientific Instruments* 77, 73101 (2006).

R. Furstenberg and J. O. White, "Phase correction of interferograms using digital all-pass filters", *Applied Spectroscopy* 59, 316-321 (2005).

R. Furstenberg, J. O. White, and G.L. Olson, "Spatially-resolved photoluminescence and transmission spectra of HgCdTe", *Journal of Electronic Materials* 34, 791-794 (2005).

R. Furstenberg, J. O. White and G. L. Olson: "Spatially resolved photoluminescence and transmission spectra of HgCdTe", *Journal of Electronic Materials* **34**, 791 (2005).

R. Furstenberg and J. O. White, "Phase correction of interferograms using digital all-pass filters", *Applied Spectroscopy* **59**, 316 (2004).

R. Furstenberg, J. O. White, J. H. Dinan, and G. L. Olson: "High-resolution mapping of infrared photoluminescence," *J. Electron. Mat.* **33**, 714 (2004).

S. L. Chuang and N. Holonyak, Jr., "Efficient quantum-well to quantum-dot tunneling: analytical solutions," *Appl. Phys. Lett.*, 80, 1270 (2002).

W. Y. Ruan and Yia-Chung Chang, "Inverted ordering of acceptor bound exciton states in Si: the role of electron-hole correlation," *Phys. Rev. B.* **69**, 245206 (2004).

X. B. Zhang, R. D. Heller, J. H. Ryou, R. D. Dupuis, G. Walter, and N. Holonyak, Jr., "Growth of InP self-assembled quantum dots on strained and strain-relaxed $\text{In}_x(\text{Al}_{0.6}\text{Ga}_{0.4})_{1-x}\text{P}$ matrices by metalorganic chemical vapor deposition," *J. Appl. Phys.*, 100, 043511 (2006).

X. B. Zhang, J. H. Ryou, R. D. Dupuis, A. Petschke, S. Mou, S. -L. Chuang, C. Xu, and K. -C. Hsieh, "Metalorganic chemical vapor deposition growth of high-quality InAs/GaSb Type II superlattices on (001) GaAs substrates," *Appl. Phys. Lett.* 88, 072104 (2006).

X. B. Zhang, J. H. Ryou, R. D. Dupuis, S. Mou, S. -L. Chuang, C. Xu, and K. -C. Hsieh, "Metalorganic chemical vapor deposition of metamorphic InAs-GaSb superlattices on (001) GaAs substrates for mid-IR photodetector applications," *J. Crystal Growth* 287, 545 (2006).

X. B. Zhang, J. H. Ryou, R. D. Dupuis, L. He, R. Hull, G. Walter, and N. Holonyak, Jr., "Effect of thin strain-compensated $\text{Al}_{0.6}\text{Ga}_{0.4}\text{P}$ layers on the growth of multiple-stacked $\text{InP}/\text{In}_{0.5}\text{Al}_{0.3}\text{Ga}_{0.2}\text{P}$ quantum dots," *J. Electron. Mater.* 35, 701 (2006).

X. B. Zhang, J. H. Ryou, R. D. Dupuis, G. Walter, and N. Holonyak, Jr., "Metalorganic chemical vapor deposition growth and characterization of InGaP/GaAs superlattices," *J. Electron. Mater.*, 35, 705 (2006).

X. B. Zhang, J. H. Ryou, R. D. Dupuis, L. He, R. Hull, G. Walter, and N. Holonyak, Jr., "Tuning the morphology of InP self-assembled quantum

structures grown on InAlP surfaces by metalorganic chemical vapor deposition,” *Appl. Phys. Lett.* 86, 233105 (2005).

X. B. Zhang, J. H. Ryou, R. D. Dupuis, G. Walter, and N. Holonyak, Jr., “Interface alloy mixing effect in the growth of self-assembled InP quantum dots on InAlGaP matrices by metalorganic chemical-vapor deposition,” *J. Appl. Phys.* 98, 063501 (2005).

Y. C. Chang, R. B. Jame, and J. Davenport, “Symmetrized-basis LASTO calculations of defects in CdTe and ZnTe”, *Phys. Rev. B*, 73, 035211 (2006).

Z. H. Zhang and K.Y. Cheng, C.F. Xu, and K.C. Hsieh, “Defect-Free 100-Layer Strain-Balanced InAs Quantum Dot Structure Grown on InP Substrate,” *Appl. Phys. Lett.*, 89, 063115 (2006).

Z. H. Zhang and K. Y. Cheng, “Growth of High Quality InAs Quantum-Dot Multi-Layer Structures on InP for Infrared Photodetector Applications”, *J. Vacuum Sci. Technol. B*24, 1656-1659 (2006).

Z. H. Zhang and K. Y. Cheng, “Growth of High Optical Quality InAs Quantum-Dots on AlGaInAs/InP Double Heterostructures”, *J. Vacuum Sci. Technol. B* 23, 1125-1128 (2005).

Z. H. Zhang, K. Y. Cheng, C. F. Xu, and K. C. Hsieh, “Defect-Free 50-Layer Strain-Balanced InAs Quantum Dots Grown on InAlGaAs/InP for Infrared Photodetector Applications”, *J. Crystal Growth*, 278, 61-66 (2005).

Z. H. Zhang and K. Y. Cheng, “temperature stabilized 1.55 μm photoluminescence in InAs quantum dots grown on InAlGaAs/InP”, *J. Vac. Sci. Technol. B*, 22, 1508 (2004).

Z. H. Zhang, G. W. Pickrell, K. L. Chang, H. C. Lin, K. C. Hsieh, and K. Y. Cheng, “Surface morphology control of InAs nanostructures grown on InGaAs/InP,” *Appl. Phys. Lett.* 82, 4555, (2003).

Z. H. Zhang and K. Y. Cheng, “Growth of uniform InAs quantum dots on InGaAs surface structure modified superlattices on InP,” *Appl. Phys. Lett.* 83, 3183, (2003).

(c) Papers published in non-peer-review journals or in conference proceedings:

C. Xu and K. C. Hsieh, “In-situ TEM study of HgCdTe decomposition,” 24th Army Science Conference.

E. Hoffman and S. L. Chuang, “Theory for intersubband absorption in quantum dots,” *Physics and Simulation of Optoelectronic Devices XII*, SPIE vol. 5349, San Jose, CA, Jan. (2004).

J. V. Li, S. L. Chuang, O. V. Sulima, and J. A. Cox, “XPS and AES study of $(\text{NH}_4)_2\text{S}$ passivation effect on InGaAsSb material for AlGaAsSb/InGaAsSb/GaSb photodiodes with polyimide encapsulation,” The 6th Mid-Infrared Optoelectronics Material and Device Conference, St. Petersburg, Russia (2004).

J. Velev and Y. C. Chang, “Giant magnetoresistance in nanowires,” APS annual meeting, March (2002).

M. Lerttamrab, S. L. Chuang, R. Q. Yang, and C. J. Hill, "Linewidth enhancement factor of a type-II quantum-cascade laser," CLEO 2004, Paper CMR5 (2004).

R. Furstenberg and J.O. White, "Error-free phase correction of interferograms using digital all-pass filters," The Third International Conference on Advanced Vibrational Spectroscopy, Delavan, WI, 14-19 August (2005).

R. Furstenberg and J. O. White, "Spatially resolved photoluminescence and absorption spectra of CdZnTe and HgCdTe," 2004 U.S. workshop on the physics and chemistry of II-VI materials, Chicago, October 5-7 (2004).

R. Furstenberg, J.O. White (UIUC) and J.H. Dinan (U.S. Army CECOM NVESD): "High-resolution mapping of infrared photoluminescence," 2003 Surface Analysis Conference.

R. Furstenberg, J.O. White (UIUC), J.H. Dinan (U.S. Army CECOM NVESD) and G.L. Olson (HRL Laboratories): "High-resolution mapping of infrared photoluminescence," 2003 U.S. Workshop on the Physics and Chemistry of II-VI Materials.

S. L. Chuang and N. Holonyak, Jr., "Efficient quantum-well to quantum-dot tunneling," APS annual meeting, March (2002).

S. W. Chang, S. L. Chuang, and N. Holonyak, Jr., "Quantum-well to quantum-dot phonon-assisted tunneling," *Physics and Simulation of Optoelectronic Devices XII*, SPIE vol. 5349, San Jose, CA, Jan. (2004).

Y. C. Chang and H. Kim, "Ab initio studies of defects in CdTe and HgTe with symmetrized basis," APS annual meeting, March (2006).

(d) Papers presented at meetings, but not published in conference proceedings:

None

2. Demographic Data for this Reporting Period:

(a) Number of Scientists Supported by this agreement (decimals are allowed): 1

(b) Number of Inventions resulting from this agreement: None

(c) Number of PhD(s) awarded as a result of this agreement: 4

(d) Number of Bachelor Degrees awarded as a result of this agreement: None

(e) Number of Patents Submitted as a result of this agreement: None

(f) Number of Patents Awarded as a result of this agreement: None

(g) Number of Grad Students supported by this agreement: 8

(h) Number of FTE Grad Students supported by this agreement: 8

(i) Number of Post Doctorate Students supported by this agreement: 1

(j) Number of FTE Post Doctorate Students supported by this agreement: 0

(k) Number of Faculty supported by this agreement: 6

(l) Number of Other Staff supported by this agreement: None

(m) Number of Undergrads supported by this agreement: None

(n) Number of Master Degrees awarded as a result of this agreement: 2

3. Demographic Data for the life of this agreement:

- (a) Number of Scientists Supported by this agreement (decimals are allowed): 2
- (b) Number of Inventions resulting from this agreement: 1
- (c) Number of PhD(s) awarded as a result of this agreement: 7
- (d) Number of Bachelor Degrees awarded as a result of this agreement: 1
- (e) Number of Patents Submitted as a result of this agreement: 1
- (f) Number of Patents Awarded as a result of this agreement: 1
- (g) Number of Grad Students supported by this agreement: 14
- (h) Number of FTE Grad Students supported by this agreement: 14
- (i) Number of Post Doctorate Students supported by this agreement: 1.5
- (j) Number of FTE Post Doctorate Students supported by this agreement: 0.5
- (k) Number of Faculty supported by this agreement: 8
- (l) Number of Other Staff supported by this agreement: None
- (m) Number of Undergrads supported by this agreement: None
- (n) Number of Master Degrees awarded as a result of this agreement: 3
- (o) Honors conferred and Award received by scientific personnel supported by this agreement
 - N. Holonyak Jr., Global Energy Award, Russia, 2003
 - N. Holonyak Jr., IEEE Medal of Honor, 2003
 - R. D. Dupuis and N. Holonyak Jr., Medal of Technology, White House, 2003
 - K. Y. Cheng: Fellow of the American Association for the Advancement of Science, 2003.
 - S. L. Chuang, Fellow of American Physical Society, 2003.
 - Milton Feng, Fellow of the Optical Society of America, 2003.
 - N. Holonyak Jr., Lemelson-MIT Prize, 2004.
 - N. Holonyak Jr., Washington Award, 2004.
 - N. Holonyak Jr., Von Hippel Award, Materials Research Society, 2004.
 - R. D. Dupuis, Distinguished Alumnus Award, College of Engineering, University of Illinois at Urbana-Champaign, 2004.
 - R. D. Dupuis, John Bardeen Award, The Minerals, Metals and Materials Society, 2004.
 - S. L. Chuang, Distinguished Lecture Award, IEEE LEOS, 2004-2006.
 - S. L. Chuang, Engineering Excellence Award, Optical Society of America, 2004.

4. Report of Inventions:

S. L. Chuang, J. V. Li, and R. Q. Yang, "Room temperature mid-infrared photovoltaic detectors based on type-II interband cascade structure," *US provisional patent*, 2004.

5. Advanced Degrees Earned:

M.S. : 4 Ph.D. : 7

J. V. Li, "Antimonide-based type-II quantum well infrared photodetectors," Ph.D. thesis, UIUC (Advisor, S. L. Chuang), 2005. (Joined JPL).

Maytee Lerttamrab, Ph.D. thesis, UIUC (Advisor, S. L. Chuang), 2006.
 (Joined Sandia National Lab)

R. Furstenberg, "Photoluminescence of defects in Mercury Cadmium Telluride," Ph.D. thesis, UIUC (Advisor, Y. C. Chang with Jeff White), 2006. (Joined NRL)

Z. H. Zhang, Ph. D. thesis, UIUC (Advisor, K. Y. Cheng), 2005. (Joined Applied Materials)

G. Qian, Ph.D., UIUC (Advisor, Y. C. Chang), 2005.

R. Heller, Ph.D., University of Texas at Austin (Advisor, R. Dupuis), 2003.

J. Velev, "Giant magnetoresistance in multilayers," Ph.D. thesis, UIUC, (Advisor, Y. C. Chang), 2002.

6. Technology Transfer

- Collaboration with Dr. Yang in Jet Propulsion Lab on the invention of interband cascade detector.
- Collaboration with Dr. Cory in Jet Propulsion Lab on InAs/InGaSb type-II superlattice photodiodes.
- Collaboration with Astro Power Inc. on the passivation of AlGaAsSb/InGaAsSb/GaSb photodiodes
- Collaboration with Naval Research Laboratory on the processing and passivation of Sb-based type-II superlattice photodetectors.
- Contacts with Amy Buell at Raytheon (PL mapping of FPAs)
- Collaboration with J.H. Dinan at U.S. Army CECOM NVESD (imaging CZT substrates and SWIR material), and G.L. Olson, Brett Nosh, J. Jensen at HRL Laboratories.

Table of Contents

Report Documentation pages (form 298 and continuation pages)	1
List of papers submitted or published	3
Demographic Data for this Reporting Period	6
Demographic Data for the life of this agreement	6
Report of Inventions	7
Advanced Degrees Earned	7
Technology Transfer	8
Table of contents (this page)	9
Abstract, Problems Studied and Personnel	10
Summary of the most important results	11
Task 1: HgCdTe Photodetectors	11
Task 1A: TEM study of defects in MCT	11
Task 1B: Theoretical modeling of defects in MCT	13
Task 1C: NSOM study of defects in MCT	16
Task 2: Antimony-based Type-II Infrared Photodetectors	20
Task 2A: Type-II Infrared Photodetectors based on MBE	20
Task 2B. InP/InAlGaP Quantum Dot Intersubband Transition Structures and InAs/GaSb Type-II Superlattice Structures for Mid-IR Photodetector Applications Grown by Metalorganic Chemical Vapor Deposition	23
Task 3: Quantum-Dot Infrared Photodetectors	27

Abstract, Problems Studied and Personnel:

Principle Investigator: S. L. Chuang, University of Illinois, Department of ECE, 1406 West Green Street, Urbana, IL 61801. Phone: 217-333-3359. Fax: 217-333-5701.
E-mail: s-chuang@uiuc.edu

Task 1: Investigation of HgCdTe Defects

Principle Investigators: Y. C. Chang, Dept. of Physics, UIUC
K. C. Hsieh, Dept. of ECE, UIUC
J. O. White, MRL, UIUC (now with ARO)
Graduate Students: C. Xu, R. Furstenberg, J. Velez, H. Kim, G. Qian
Visitor: Prof. W. Y. Ruan (part time)

Task 2: Sb-based Type-II Superlattice Photodetectors

Principle Investigators: S. L. Chuang, Dept. of ECE, UIUC
Russell Dupuis, Dept of ECE, GIT
Graduate Students: J. V. Li, S. Mou, A. Petschke, UIUC
Post-doctoral researcher: X. Zhang, GIT
Research engineer: J. H. Ryou, GIT

Task 3: Quantum-Dot Infrared Photodetectors

Principle Investigators: K. Y. Cheng, Dept. of ECE, UIUC
Graduate Students: Z. Zhang

Fundamental research issues on infrared photodetectors are reported. These include the following:

Task 1. HgCdTe (MCT) defect study – Continuing the research on degradation of MCT, we explore the size changing of the dislocation loops and the effect of low-dose electron beam irradiation during TEM analysis. Self-energy correction is included to calculate the MCT defect states. For the photoluminescence image, we correlate the PL images from MCTs and their CZT substrates.

Task 2. Antimony-based type-II superlattice (T2-SL) photodetectors – We explored the temperature dependent and noise current characteristics of interband cascade detectors (ICDs). We also acquired type-II superlattice photodiodes from Jet Propulsion Lab and obtained a high detectivity of $5.23 \times 10^{10} \text{ cmHz}^{1/2}/\text{W}$ at 77 K with device of 10.5 μm cutoff wavelength. Moreover, MOCVD growth of InAs/GaSb type-II superlattices was explored with substrates of both GaSb and GaAs.

Task 3. Quantum dot infrared photodetectors (QDIPs) – Our work has been focused on the growth and fabrication of high performance QDIP devices based on technologies developed. A defect-free 100-period InAs QD structure has been demonstrated. For InAs QDIPs grown on InP substrates by molecular beam epitaxy (MBE), a peak detectivity of $2.1 \times 10^9 \text{ cmHz}^{1/2}/\text{W}$ was achieved at a bias voltage of 0.8V.

Summary of the Most Important Results

Task 1: HgCdTe Photodetectors – Defects and Interface Issues

Task 1A: TEM study of defects in MCT

Principle Investigator: K. C. Hsieh, Dept. of ECE, UIUC
Graduate Student: C. Xu

Summary of previous annual reports: degradation of the MCT samples having Hg content around 65%

In our previous annual reports, we have shown certain HgCdTe (MCT) samples degraded in air at room temperature. We monitored the degradation of both bulk and thin film (in electron-transparent TEM samples) MCT. We have employed several techniques including TEM, SEM, energy-dispersive x-ray spectra (EDXS), X-ray diffraction analysis (XRD) and AFM to verify our results. Some of these techniques are non-destructive to the examined MCT samples. To positively identify and verify the time dependence of mercury loss and tellurium precipitation in MCT we have made our best effort to eliminate the possible artificial effect during sample preparation. Techniques such as lower sample temperature below -100 °C during ion milling and low voltage and low angle cleaning after perforation were applied to every TEM sample prepared.

So far we have tracked the structural change for samples stored in a dry box at room temperature over multiple years. As a result of the structural change tellurium precipitates about 500 Å in size and $5 \times 10^{13}/\text{cm}^2$ in density formed in the MCT layer. Te precipitates have also been found in other but not all samples. An interesting correlation between the formation of Te precipitates and AFM morphology is noticed. Degraded samples, which have Te precipitates in the bulk, show a corrugated AFM morphology. In contrast, the surface morphology appears monotonous for samples, which don't have Te precipitates in the bulk. We also noticed the existence of Te precipitates in the degraded MCT samples by using XRD analysis, which is also a non-destructive measurement.

Similar degradation resulting from Hg loss and resulting in Te precipitation in MCT layers has been induced in-situ by exposing TEM thin sections with excessive electron beam, whose current intensity is about 30 times over its general operation range. The whole structural degradation takes place in a second. However, a great similarity is drawn between the microstructure of samples degraded in-situ and the one slowly transformed in air. This kind of similarity indicates a possible degradation mechanism in which Hg loss and MCT decomposition are the key processes.

In the meanwhile, we applied the SEM with EDXS to surfaces of the bulk MCT samples which were identified with degradation according to TEM and AFM measurements. By comparing the chemical composition of Hg, Cd and Te from different position on the degraded MCT samples, the spatial non-uniformity of chemical composition was clearly observed when the incident beam energy reduced to 5 KeV. In order to verify our observation on the MCT samples, a stoichiometric GaAs sample was measured under same condition and did not show any spatial variation.

New observation: size changing of the dislocation loops and the effect of low-dose electron beam irradiation during TEM analysis

Dislocation loops with various sizes from 100 to 500 Å were found in three MCT samples 3714, 3786 and 3810 in November 2004, when we received and examined these samples under TEM at the first time. In order to characterize the time variation of these dislocation loops, we prepared and examined another set of samples in July 2006.

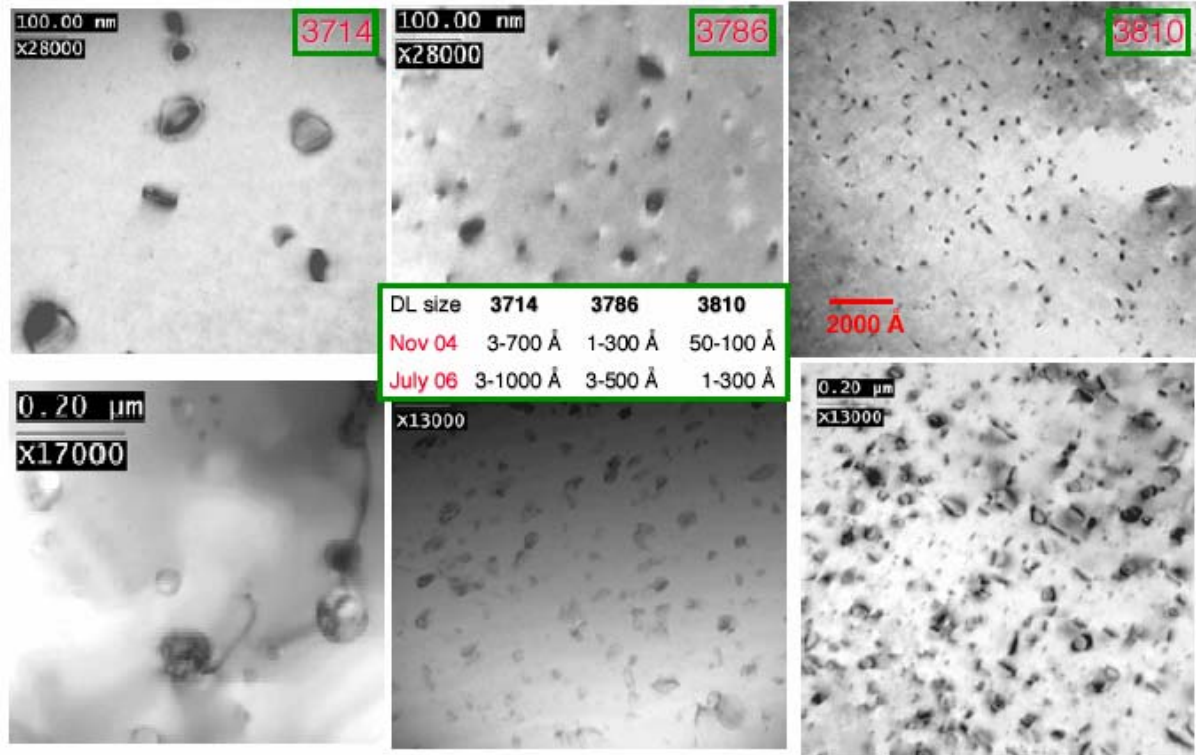


Fig. 1. TEM images of MCT degraded in air at room temperature. From left to right are samples 3714, 3786 and 3810. Three images on top were taken in November 2004 and three on bottom were taken in July 2006. (Please notice that the magnifications are not the same for these images)

Fig. 1 shows the development of those dislocation loops in all three MCT samples. For sample 3714, some dislocation loops developed to Te precipitates, which were verified by EDXS. For samples 3786 and 3810, sizes of those dislocation loops expand from 50-100 Å and 100-300 Å to 100-300 Å and 300-500 Å respectively. Given the possible time frame of growth of these three samples, we believed that the dislocation loops grow in size with time and develop to Te precipitates due to Hg loss.

As previously mentioned, excess electron beam irradiation was applied to study the in-situ structure changing of TEM thin film and the possible degradation mechanism. In addition, we also want to evaluate the effect of low-dose electron beam irradiation during general TEM analysis. In this consideration, two TEM samples were prepared for sample 3714 in November 2005. Both of them are pre-thinned and ion-milled in the identical condition. One sample was examined under TEM right after preparation and the other was kept in the air at room temperature. About six months later, both samples were checked using TEM.

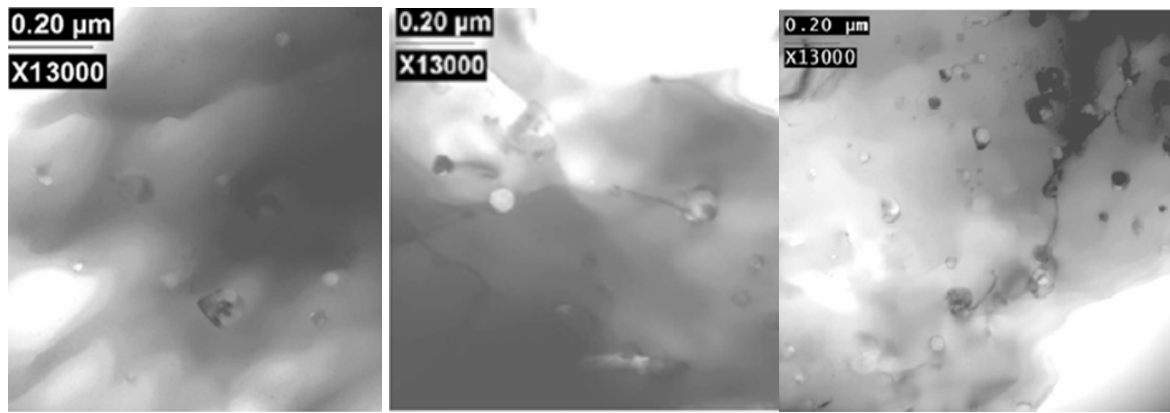


Fig. 2. TEM images of MCT samples (All from sample 3714). From left to right are sample examined right after preparation, the same sample reexamined 6 months later and sample kept in the air and examined 6 months after preparation.

From Fig. 2, TEM image of sample examined right after preparation shows that some dislocation loops and Te precipitates formed inside the sample. The same sample reexamined 6 months later and some threading dislocations pinned with Te precipitates formed. This finding is consistent with our previous study on other TEM samples from different sources. When we examined the sample sitting in the air for 6 months after preparation, the similar threading dislocations were observed with comparable density and size. At this point, threading dislocations are formed in both samples whether or not exposed to low-dose electron beam irradiation before. We conclude that the effect of low-dose electron beam irradiation to the formation of threading dislocations is thus limited to a low level of affecting our TEM analysis.

Task 1B: Theoretical modeling of defects in MCT:

Principle Investigator: Y. C. Chang, Dept. of Physics, UIUC
 Visitor: Prof. W. Y. Ruan (part time)
 Graduate Students: J. Velev, H. Kim, G. Qian

Highlights of accomplishments:

- Studied neutral, singly and doubly charged Hg/Cd vacancy and defect complexes in HgTe and CdTe with large supercells via both plane-wave pseudopotential and full potential LASTO calculations .
- We have studied the effects of quasi-particle self-energy correction for large supercell systems from first principles. The same method can be applied to study the self-energy correction of defect levels, which is essential for HgCdTe.
- We have performed ab initio calculations of the excitation spectra of large supercell systems, including the self-energy correction and excitonic effect. This method can be applied to calculate defect induced optical absorption spectra

Our Major Findings:

- Both plane-wave pseudopotential and full potential LASTO calculations yield similar results.

- Te atoms surrounding vacancy relax inward around 3% when the second-neighbor Hg/Cd atoms are fixed and around 10% when the second-neighbor Hg/Cd atoms are also relaxed (which relax inward by about 2%).
- Jahn-Teller distortion is negligible for singly-charged and neutral vacancies in CdTe.
- The new method developed for calculating self-energy correction and excitonic effect in large supercells yield results in good agreement with experiment for SiH clusters.
- For Cd vacancies in CdTe, there is a defect level (of Γ_8 symmetry) above the valence band maximum of CdTe by about 0.1 eV. However, for Hg vacancies in HgTe, the same defect level is buried deep (about 0.4 eV) into the valence bands of HgTe.

Summary of main results:

Our major goal is to study the electronic structures of defect complexes (vacancies, vacancy-donor pair, and dislocations) in semiconductors and their effect on carrier capture rates, an important limiting factor for HgCdTe IR detectors. We have performed ab initio pseudopotential calculations of the total energy and atomic relaxation of neutral and charged Cd vacancies in CdTe and Hg vacancies in HgTe using both pseudopotential and full potential linearized augmented Slater-type orbital (LASTO) methods developed within our group (with supercells of 8, 16, 32, 54, and 64 atoms). Our method takes advantage of the high point symmetry of the system. Using symmetrized basis function allows us to reduce both the CPU time and memory requirement substantially. The two independent calculations give consistent results, which lend to credibility to the calculation.

The main results are summarized in tables below.

Table I. The fractional change in Te-vacancy distance relative to their initial bond lengths for first neighbor (δd_1) and second neighbor (δd_2) and energy lowered due to relaxation ΔE for neutral (V^0), singly-charged (V^{-1}) and doubly-charged (V^{-2}) Cd vacancies in CdTe calculated via a 64 atom supercell. All energies are in eV. The values outside (inside) parentheses are results obtained with (without) the inclusion of spin-orbit interaction.

	V^0	V^{-1}	V^{-2}
δd_1	-0.092 (-0.089)	-0.089 (-0.083)	-0.088 (-0.087)
δd_2	-0.024 (-0.023)	-0.025 (-0.024)	-0.027 (-0.027)
ΔE (eV)	0.299 (0.257)	0.324 (0.287)	0.375 (0.360)

Table II. Energies (in eV) of defect-induced levels of Cd vacancy in CdTe obtained via (a) pseudopotential and (b) LASTO calculations. (all results include the effect of spin-orbit interaction)

a. Pseudopotential method for 64 atom supercell

State	V^0	V^{-1}	V^{-2}
Γ_6	-2.193	-2.121	-2.051

Γ_7	-0.632	-0.558	-0.476
Γ_8	0.001	0.036	0.073

b. LASTO method for 128 (54) atom supercell

State	V^0	V^{-1}	V^{-2}
Γ_6	-1.857(-2.328)	-1.815(-2.290)	-1.778(-2.219)
Γ_7	-0.460(-0.585)	-0.401(-0.522)	-0.306(-0.426)
Γ_8	0.049(0.033)	0.067(0.052)	0.111(0.093)

Table III. Semi-empirical GW correction (in eV) of defect levels relative to VBM for Cd vacancy in CdTe.

	V^0			V^{-1}			V^{-2}		
	Γ_6	Γ_7	Γ_8	Γ_6	Γ_7	Γ_8	Γ_6	Γ_7	Γ_8
Δ	0.035	0.039	0.019	0.036	0.038	0.020	0.035	0.040	0.022

Table IV. The fractional change in Te-vacancy distance relative to their initial bond lengths for first neighbor (δd_1) and second neighbor (δd_2) and energy lowered due to relaxation ΔE for neutral (V^0), singly-charged (V^{-1}) and doubly-charged (V^{-2}) Hg vacancies in HgTe calculated via a 64 atom supercell. All energies are in eV. The values outside (inside) parentheses are results obtained with (without) the inclusion of spin-orbit interaction.

	V^0	V^{-1}	V^{-2}
δd_1	-0.061 (-0.068)	-0.068 (-0.076)	-0.074 (-0.087)
δd_2	-0.013 (-0.013)	-0.013 (-0.015)	-0.013 (-0.016)
ΔE (eV)	0.180 (0.178)	0.194 (0.214)	0.210 (0.263)

Table V. Energies (in eV) of defect-induced levels of Hg vacancy in HgTe obtained via (a) pseudopotential and (b) LASTO calculations. (all results include the effect of spin-orbit interaction)

a. Pseudopotential method for 64 atom supercell

State	V^0	V^{-1}	V^{-2}
Γ_6	-2.560	-2.577	-2.590
Γ_7	-1.131	-1.126	-1.120
Γ_8	-0.984	-0.977	-0.969

b. LASTO method for 128 (54) atom supercell

State	V^0	V^{-1}	V^{-2}
Γ_6	-2.015(-2.514)	-2.056(-2.561)	-2.054(-2.592)
Γ_7	-0.700(-0.827)	-0.725(-0.836)	-0.688(-0.840)
Γ_8	-0.430(-0.620)	-0.439(-0.634)	-0.420(-0.647)

Table VI. Semi-empirical GW correction (in eV) of defect levels (relative to VBM) for Hg vacancy in HgTe.

	V^0			V^{-1}			V^{-2}		
	Γ_6	Γ_7	Γ_8	Γ_6	Γ_7	Γ_8	Γ_6	Γ_7	Γ_8
Δ	0.044	0.041	0.028	0.042	0.042	0.030	0.041	0.041	0.031

Ongoing work (to be completed in the near future):

- Develop ab initio Green's function code for studying defect complexes and capture cross-section.
- Study long-range Coulomb field for charged defects.

Task 1C: NSOM study of defects in MCT

Principle Investigator: J. O. White, MRL, UIUC
Graduate Student: R. Furstenberg

PL-mapping instrument

During this project, we designed and built an instrument for mapping photoluminescence (PL) and phototransmission (PT) from the near-IR to 13 μm , for use in conjunction with an FTIR and a grating spectrometer [1]. We believe PT can be extremely useful in determining the bandgap of MCT. It was important to add high spatial resolution for several reasons. a) In high-quality samples, the strong band-edge PL would overwhelm the emission from defects with energies close to the band edge, unless the excitation light could be concentrated on the defective region. b) A PL spectrum from a macroscopic region of the

sample would likely have multiple peaks, due to either a defect with multiple energy levels, or to multiple defects. PL mapping can help to resolve the ambiguity by showing whether the different peaks originate from the same or different regions of the sample. c) Correlating FPA performance with the PL map of an MCT film before processing requires a spatial resolution comparable to a typical pixel, ~20 μm .

MCT results

For good quality MCT, and 10-30 mW of pump light at 1440 nm, room temperature bandedge PL spectra with a SNR of 30, and a spatial resolution of 25 μm can be obtained in 30-50 s/pixel. Imaging the FWHM, for example, reveals a clear difference between as-grown and annealed pieces of the same wafer (HRL-3307). Imaging the PL peak area reveals that occasional pixel-sized areas are 20% less efficient in emitting light [2,3].

CdTe / CdZnTe results

Defects can occur during the growth of CZT films on Si, or during the polishing of bulk CZT substrates. The quality of the polish that can be obtained in the U.S. is inferior to that done routinely by Nikko Corp. of Japan. PL mapping of CZT could play an important role in the optimization of a domestic polishing capability. PL spectra acquired at 77 K display a defect band that is probably a superposition of several different emission lines. To help determine the composition of the band, spectra were also acquired at temperatures down to 9 K. They revealed that the defect band consists of three distinct transitions [4].

The shape of the emission in the 1.3 – 1.56 eV region suggests the presence of more than one transition. To determine the most appropriate model for the band, we acquired spectra at temperatures down to 9 K, where the lines are more distinct. However, phonon replicas complicate the picture, and make it necessary to model the spectra to obtain the transition energies. At low temperatures the line shape of a defect level transition is given by the Poisson distribution:

$$I(\nu - \nu_0) = \sum_{n=0}^{\infty} \frac{S^n}{n!} \exp(-S) g(\nu - \nu_0 - n\nu_{LO})$$

Where n is the number of phonons emitted at the specific transition, S is the Huang-Rhys factor, g is the lineshape of the transition, and ν_{LO} is the longitudinal phonon frequency. The model was able to reproduce the experimental spectra except at 1.54 eV, probably due to our assumption of a Gaussian broadening. The peak energies are as follows:

Table VII. Peak energies in the PL spectrum from CZT at 9.4 K.

eV	S	Origin of the peak
1.618	~0	band to band transition (e-h recombination)
1.613	~0	e-h recombination involving a shallow donor or acceptor.
1.572	0.3 \pm 0.05	transition of an electron in the conduction band to the ground state of a neutral double acceptor center, probably a Cd vacancy. [5,6]
1.567	(too weak to determine)	A transition probably similar to the 1.572eV
1.518	0.8 \pm 0.1	Unknown defect
1.500	2.2 \pm 0.1	Unknown defect
1.466	1.5 \pm 0.1	Unknown defect

The high value of S for the three low energy peaks indicates a significant amount of lattice distortion, hence these are probably complex defects. The two high energy peaks had no noticeable phonon replicas, meaning that no lattice distortion is present. As the temperature increases, the peak area rapidly decreases around 68 K, and around 36 K. We associate a decrease in PL with an increase in non-radiative combination due to thermal activation of two unknown traps [7].

We also analyzed the spatial distribution of PL spectra at 77 K, where the phonon replicas blend together and the data can be fit with a simple Gaussian for each of five transitions. The peaks can be divided into two groups that anti-correlate, as shown in the table below.

Table VIII. Spatial correlation between various peaks in the defect PL from CZT.

Correlation	1.60 eV	1.57 eV	1.51 eV	1.49 eV	1.46 eV
1.60	1.000	0.407	0.043	-0.108	0.477
1.57		1.000	-0.144	0.137	0.381
1.51			1.000	0.741	0.121
1.49				1.000	-0.077
1.46					1.000

MCT / CZT correlation results

Experiments to correlate the quality of an MCT film with the quality of the substrate were made possible by two samples of HgCdTe ($x=0.28$) epilayers grown on bulk CdZnTe, provided by Dr. J.H. Dinan. One CZT substrate was used as a substrate in the condition in which it was received from Nikko; the other was repolished in the U.S. prior to deposition. The previous report showed that the Nikko-polished sample had a higher PL intensity at all temperatures from 9-50 K, with the difference increasing with temperature.

A second type of experiment involved etching the HgCdTe with a 0.5% Br⁻ solution in Methyl-alcohol, imaging the sample after each etch, and then imaging the underlying CdZnTe, as suggested by Dr. R. deWames. The sample shown in Fig. 3 is the repolished one. The scan range is 5.2mm with 153 μ m pixels for the mid-IR maps and 38 μ m for the near-IR (i.e. CdZnTe) maps. Several features are worthwhile noting.

1. The dark area in the lower left quadrant of the MCT image (column two) is more visible in the peak position image than in the peak area image.
2. In both of the CZT images, there is a “spot” in the same location, suggesting that the MCT defect arose from a problem in the substrate. However, all the “spots” in the CZT images did not result in defects in the MCT images.
3. Some of the black areas in the CZT images are due to residual MCT.
4. There is often, but not always, a negative correlation between the features in CZT bands 1 and 2 (not including the features due to residual MCT)

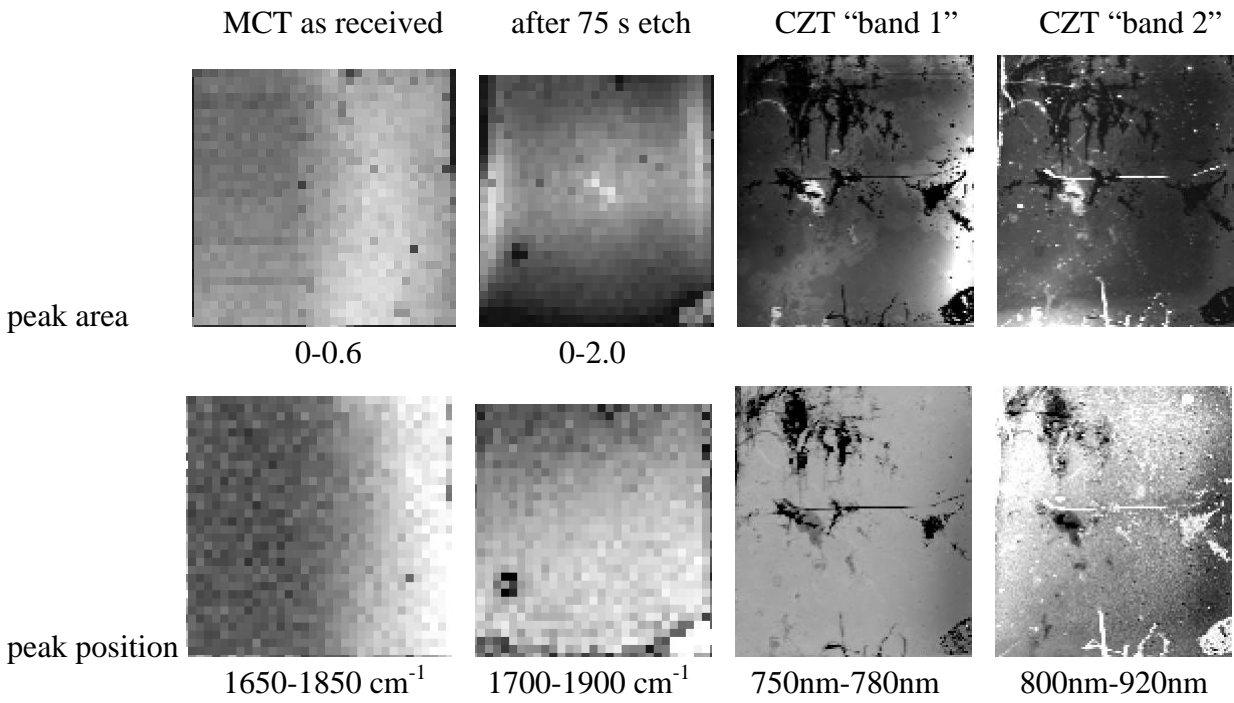


Fig. 3. PL images of an MCT film, and the underlying CZT substrate, acquired at 77 K. Scan range 5.2 mm.

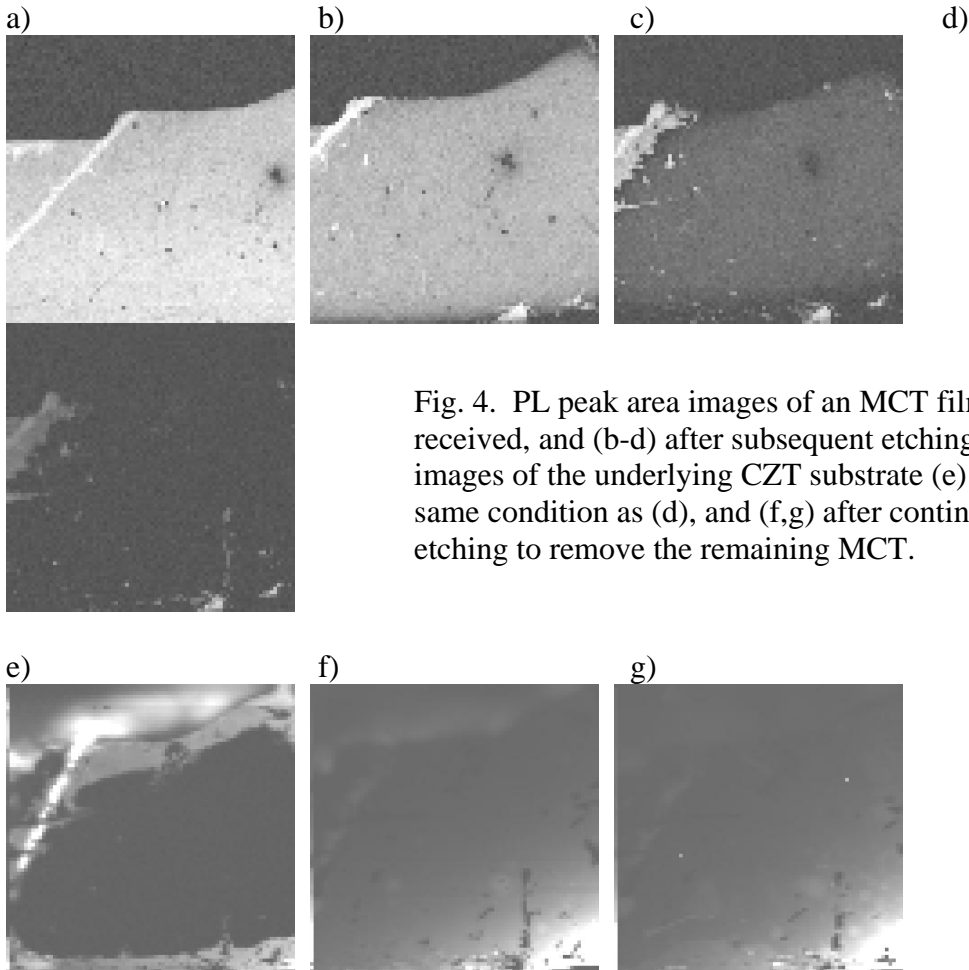


Fig. 4. PL peak area images of an MCT film (a) as-received, and (b-d) after subsequent etching. PL images of the underlying CZT substrate (e) in the same condition as (d), and (f,g) after continued etching to remove the remaining MCT.

The experiment was repeated with a higher resolution on a second piece of the same MCT sample. The scan range in all images was 2.0 mm with 25 μm pixels. Only the first MCT scan is shifted with respect to the rest.

Images (a-d) are of MCT; (e-g) are of the CZT substrate. The MCT was etched away until the PL signal was too small to measure (d). At this point, there is still some MCT left. Without etching any further, the CZT PL was imaged (e). Over most of the sample, the signal is zero because the remaining MCT is still thick enough to block the excitation laser. Only around the edges has the CZT been exposed. After additional etches, images (f-g) were acquired. Several features are worth noting.

1. The line in the top-left runs at 45° to the cleaved edge, and appears to delineate two crystalline regions of differing quality. The MCT PL to the left of this line is much brighter, as is the CZT PL signal from this region.
2. In the bottom-right there is an increase in MCT PL. There is a corresponding increase in the CZT PL signal.
3. The most obvious defect in the MCT image, the dark spot in the upper right quadrant, does not appear to have a corresponding feature in the CZT image.

References

1. R. Furstenberg, J.A. Soares, and J.O. White, *Rev. Scientific Instruments* **77**, 73101 (2006).
2. R. Furstenberg, et al., *J. Electronic Materials* **33** (6) 714 (2004)
3. R. Furstenberg, J. O. White, and G. L. Olson, *J. Electronic Materials* **34**, 791 (2005).
4. R. Furstenberg, J.O. White, J.H. Dinan, submitted to *Journal of Applied Physics*.
5. N.C. Giles-Taylor, et al., *J. Vac. Sci. Tech. A* **3**, 76 (1985).
6. F.J. Bryant, et al., *J. Phys. C* **4**, 641 (1971).
7. Krustok et al., *J. Appl. Phys.* **80**, 1757 (1996).

Task 2: Antimony-based Type-II Infrared Photodetectors

Task 2A: Type-II Infrared Photodetectors based on MBE

Principle Investigators: S. L. Chuang, Dept. of ECE, UIUC
 Graduate Students: S. Mou
 A. Petschke

Summary of previous results

■ *Discovery of interband cascade detectors (ICDs)*

We proposed and investigated a new class of mid-IR photovoltaic detector based on type-II interband cascade laser (ICL) structures, which we named the interband cascade detector (ICD). These ICDs combine the advantages of interband optical transitions with the excellent carrier transport properties of the ICL structures, leading to potentially high device performance in photovoltaic mode with low noise and normal incidence detection. The ICDs have a relatively high differential resistance R_0 at room temperature, which is 73.0 k Ω . The large differential resistance results in a relatively large product of R_0 and detector area A . *The room temperature R_0A product is 19 Ωcm^2 . This value is almost three orders of magnitude higher than that of*

commercially available n+-p PbSe photodiodes operating at room temperature.

■ *Measured minority carrier diffusion length using E-beam induced current (EBIC)*

We used the EBIC technique to investigate carrier transport characteristics in a type-II InAs/GaSb superlattice photodiode with cutoff wavelength at 7.7 μm . We used a theoretical model that includes an extended generation source and considers the entire depletion region to simulate the EBIC current on both sides of the p-n junction. The electron minority diffusion length in the p-superlattice, L_e , is extracted from the simulation, from which the electron lifetime is obtained. L_e increases from 0.275 μm at 5.3 K to 0.355 μm at 100 K. EBIC is a powerful tool to characterize infrared photodiodes and we believe *this is the first time it has been used on a type-II InAs/GaSb superlattice photodiode.*

■ *Device characterization and modeling*

During the MURI project period, we not only built up our device processing and characterization capabilities but also took it one step further and modeled the device characteristics. With the 8 band k-p method we developed, we calculated the absorption coefficient spectra. The calculated absorption spectra were compared to measured spectra and excellent agreement was found. Moreover, using parameters extracted from the EBIC measurements, we also established a photo-responsivity model to describe the quantum efficiency of the photocurrent. *Based on these models, we have the capability to design and optimize the structure of type-II InAs/GaSb superlattice photodiodes.*

■ *Device passivation using aqueous $(\text{NH}_4)_2\text{S}$ solution*

Aqueous ammonium sulfide solutions were used to passivate the mesa sidewalls of the T2-SL photodiodes. By using a 20% $(\text{NH}_4)_2\text{S}$ solution we were able to see a 400% decrease in the dark current and a 36% increase in the differential resistance. To further study the effects of sulfide passivation, EBIC experiments were performed to extract the surface recombination velocity (SRV). Using a 4% $(\text{NH}_4)_2\text{S}$ solution at room temperature for 30 minutes, *we saw a reduction of SRV by 100 times. We are the only group to report quantitative analysis on surface recombination velocity (SRV).*

New results (Aug, 2005 – Aug, 2006)

ICD temperature dependent experiments and noise measurements

We have performed device characterization of ICDs from 77 K to 300 K. Fig. 5 shows the R_0A as a function of inverse temperature on a log scale. With straight line fitting, we found the device is diffusion limited down to 180 K with an activation energy of 290 meV, which is close to the measured bandgap energy at 180 K (307 meV). From 180 K to 120 K, the device is generation-recombination limited with an activation energy of 132 meV, around half of the bandgap energy. The R_0A at 77 K is approximate $10^7 \Omega\text{cm}^2$, which is the highest among Sb-base photodiodes with similar cutoff wavelengths.

The dominant noise mechanism of a photovoltaic detector is usually Johnson noise, $\sqrt{\langle i_n^2 \rangle / \Delta f} = \sqrt{4kT/R_0}$, because there is no dark current at zero bias. Because ICDs are photovoltaic, it was hypothesized that Johnson noise is the principal noise mechanism of these devices. To test this hypothesis, we measured the noise using an EG&G 7220 digital lock-in amplifier at different frequencies. The results are shown in Fig. 6 for three devices with

different zero bias resistances. These devices have comparable R_0A products but different areas. Below roughly 6 kHz the 1/f noise is dominant. Above this frequency, the measured noise is very close (within a factor of 2) to the Johnson noise limit. This justifies our use of the Johnson noise and R_0A as a measure of the noise for ICD devices.

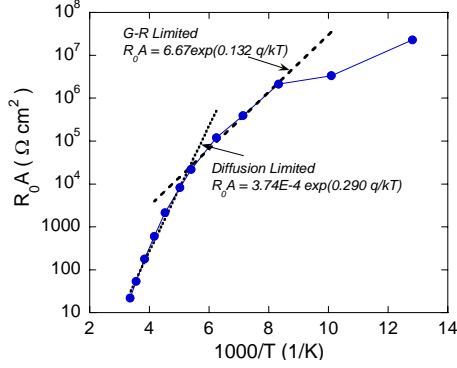


Fig. 5. Arrhenius plot of an ICD device. The device is diffusion limited down to 180 K.

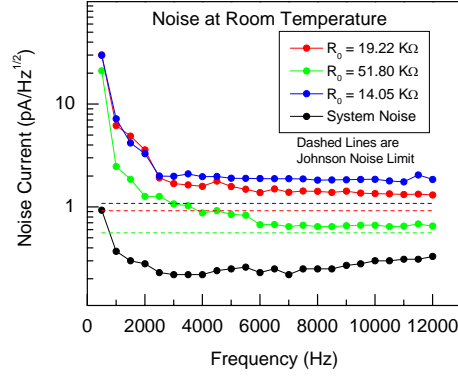


Fig. 6. Noise current at room temperature for 3 devices. The Johnson noise limits are shown as dashed lines. The measured noise is within a factor of 2 of the theoretical limit.

InAs/GaSb type-II superlattice photodiodes provided by Jet Propulsion Lab (JPL)

We received p-i-n InAs/GaSb type II SL photodetectors grown by Dr. Cory Hill at JPL. These devices were designed to have a cutoff wavelength of 10 μm . Devices were fabricated into 100 μm x 100 μm to 400 μm x 400 μm mesas using standard photolithography and wet etching techniques. No surface passivation was used. Sample Sb1030 consisted of an InAs (44 \AA)/GaSb (22 \AA) SL with an 80 period/200 period/80 period p-i-n structure. The responsivity and photoluminescence (PL) are given in Fig. 7 for a 400 μm x 400 μm mesa device. The responsivity was measured using a Bomem DA8 FTIR and calibrated using a Mikron M305 blackbody source and Stanford Research SR530 lock-in amplifier. The PL was measured using Nicolet 670 FTIR with an MCT detector. The double modulation technique with the help of a lock-in amplifier was used in order to suppress the 300K background radiation. The device has a peak responsivity of 2.3 A/W. The cutoff wavelength and PL peak both agree with the theoretical cutoff. Fig. 8 shows the Arrhenius plot of the same device. The device is diffusion limited down to 77 K where $R_0A = 2.2 \text{ } \Omega\text{-cm}^2$. Assuming the device is Johnson noise limited, the D^* is $5.23 \times 10^{10} \text{ cmHz}^{1/2}/\text{W}$ at 77 K, which is close to the state of the art for that cutoff wavelength.

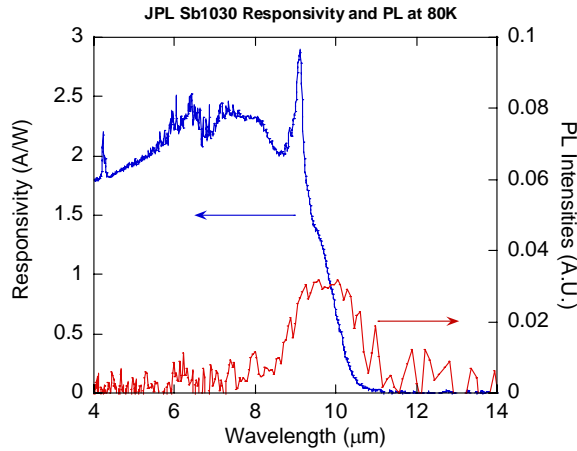


Fig. 7. Responsivity and PL for device Sb1030 ($R_0A = 2.2 \Omega - \text{cm}^2$).

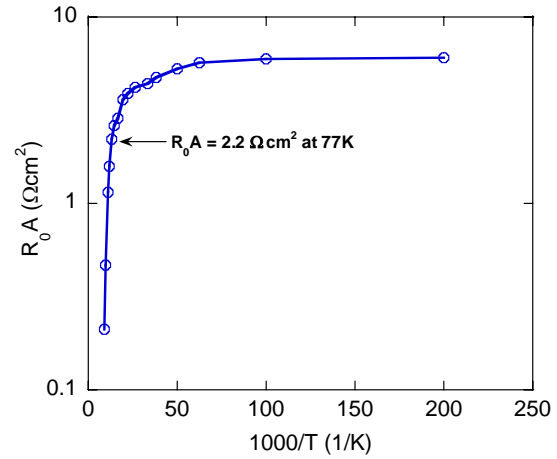


Fig. 8. Arrhenius plot of device Sb1030. The device is diffusion limited down to 77 K.

With the help of PL, we also explored the uniformity of a type-II superlattice sample. The inset of Fig. 9 shows two PL spectra at 5 K for different positions on a sample (JPL Sb1094). Though the peak energies of these two spectra are the same, the bandwidths are obviously different. By taking temperature dependent measurements on the spot with a wider spectrum, we found a kink around 80 K. It is believed the PL is dominated by defect related transitions below 80 K and then becomes band-to-band transition dominated above 80 K. This example illustrates the capability of using FTIR PL for characterizing mid-infrared photodetectors.

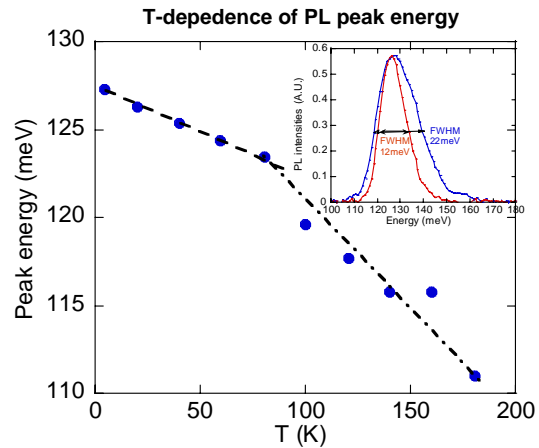


Fig. 9. The PL peak energy at various temperatures. The inset shows two PL spectra at 5K for different positions on a sample.

Task 2B. InP/InAlGaP Quantum Dot Intersubband Transition Structures and InAs/GaSb Type-II Superlattice Structures for Mid-IR Photodetector Applications Grown by Metalorganic Chemical Vapor Deposition

Principal Investigator: Russell Dupuis, Dept of ECE, Georgia Institute of Technology
 Post-doctoral researcher: X. Zhang, GIT
 Research engineer: J. H. Ryou, GIT

Under the ARO MURI program for the fundamental research on infrared (IR) photodetectors, Dupuis' group at Georgia Institute of Technology has focused on the following two structures for mid-IR photodetectors grown by metalorganic chemical vapor deposition (MOCVD): (1) InP/InAlGaP quantum-dot (QD) intersubband transition structures from year 1 (2002) to year 3 (2004) and (2) InAs/GaSb type-II superlattice structures from year 3 (2004) to year 5 (2006). This report will first summarize the major contributions and the technical

achievements in the fundamental understanding and device development of the IR photodetector structures during the year 1 and year 4 and then describe the research activities and achievements of year 5.

InP Quantum Dot Intersubband Photodetectors (QDIPs)

The quantum-dot intersubband photodetectors (QDIPs) allow normal incidence radiation detection and potentially have high temperature operation capabilities due to the reduced dark current. QDIP structures also have a long intersubband relaxation time, resulting in larger photocurrent than quantum-well intersubband photodetector (QWIP) structures. However, to realize the practical photodetectors, limited detectivity per each QD layer due to its small active volume and non-uniform size distribution needs to be improved. To overcome the limited detectivity of each QD layer, (i) QD morphology, such as size uniformity, density control, and spatial distribution of QDs, needs to be improved by novel growth technology development and (ii) QD layers should be stacked with multiple layers to obtain larger active volume per area. For the stacked QD layers, only limited number of layers can be grown without defect generation due to the accumulated strain in self-assembled QD (SAQD) structures by strain-induced Stranski-Krastanow growth mode. Therefore, the growth of QDIP structures consisting of multiple stacks of QD layers having the uniform size and spatial distribution and higher density without generating defect by strain relaxation is a critical and challenging issue in the development of QDIPs.

Dupuis' group employed InP/InAlGaP QD heterostructures for QDIP structures. For the development of InP QD morphology control for QDIPs, the effects of various growth parameters on QD morphology were studied, such as growth temperature, growth rate, and V/III ratio during the QD growth. The strain states and initial surface morphology of InAlGaP layer, the Si delta doping, and the modulation doping were also studied in terms of morphology mainly for density and spatial distribution of QDs as well as optical properties. The systematic studies on InP QD morphology and optical properties were valuable to understand InP SAQD growth and to optimize QDIP structures. After the optimization of QD morphology for the individual layer growth, the growth of multiple-stacked InP QDs were studied. 30 stacks of vertically aligned InP QD layers were grown. Also, by introducing a thin AlGaP tensile strained layer (~1.5 ML thick) in the center of the InAlGaP spacers to compensate the compressive strain generated by the underlying QDs, 50-stacked InP QDs with good morphology and spatially uniform luminescence have been realized.

Type II Superlattice Photodetectors (T2SLPs)

InAs/GaSb type-II superlattices (SLs) are a promising material system for mid-IR applications. In comparison to HgCdTe-based photodetectors and QWIPs, the type-II SL photodetectors (T2SLPs) have the flexibility in bandgap engineering, which enables one to design the bandgap over a wide IR range. Furthermore, the T2SLPs have advantages of high temperature operation due to the reduced Auger recombination rate. Also, the band-to-band tunneling current is intrinsically small due to the larger electron effective mass of SL structures than that of HgCdTe materials. When properly designed, these type-II SLs are predicted to have absorption coefficients comparable to that of HgCdTe materials. So far, the achievements in photodetectors are mostly reported by molecular beam epitaxial (MBE) growth. Our target in this program is to realize InAs/GaSb SL-based photodetectors which is grown by metalorganic chemical vapor deposition (MOCVD). GaSb growth by MOCVD has several fundamental differences compared to III-As or III-P compounds: low melting point of III-Sb materials, low equilibrium vapor pressure of Sb, and lack of stable hydride precursor for Sb. In

addition to different growth chemistry of GaSb layer, T2SLP structures require both anion and cation switching on the interface of the structures, which make interface switching and quality control challenging. Also, strain management for the mismatched SL structure growth is important for high quality T2SLP structure growth, since InAs is lattice mismatched to the GaSb layer or substrate by -0.59% and GaSb is lattice mismatched to the GaAs substrate by 7.8%.

Dupuis' group has demonstrated SL structures grown on both GaAs and GaSb substrates with good surface and structural properties. In the past year, we have systematically investigated the growth of InAs/GaSb SLs and the 100-period SLs with structural and absorption similar to those of high quality SLs reported by MBE growth have been realized. We first started with the growth of InAs-GaSb SLs on GaAs substrates. The benefit of using a GaAs substrate is that (i) GaAs substrates are cheaper and higher quality and (ii) GaAs semi-insulating substrates are easy to obtain and transparent to mid-IR wavelength region. T2SLP structures on GaAs substrates employed a buffer layer structure consisting of a low-temperature (LT) GaSb layer followed by a high-temperature (HT) GaSb layer. Having optimized the growth of GaSb using the LT nucleation layer technique, we optimized the growth of InAs and InAs/GaSb SL structure by altering growth parameters. We found that the flow rate of TMSb used to passivate the GaSb surface during the cooling before the growth of InAs strongly affects the nanopipe formation. This suggests that formation of Sb clusters or In(Ga)Sb compounds at the GaSb/InAs interface is the source of nanopipes. After the optimization of the growth of the InAs/GaSb SL, for example, $T_g=500\text{ }^\circ\text{C}$ with reduced growth rate of 3 nm/min. for GaSb, 100-period T2SLP structure was grown and the structure was characterized by structural (AFM, XRD, and TEM) and optical (FTIR spectrometry) characterization techniques. The absorption coefficient extracted from the FTIR transmission spectra measured at 78 K shows cut off wavelength, λ_c of 7.5 μm . However, due to the large lattice mismatch between the GaAs substrate and the GaSb buffer layer, threading dislocation density were found to be as high as $1\times 10^8\text{ cm}^{-2}$, which can be detrimental to the device performance.

Our research activities performed in this program during 2006 have focused on (1) the growth and characterization of high quality InAs/GaSb T2SLP structures on GaSb substrate; (2) the effect of strain-balance layer in SL structures; (3) the demonstration of T2SLPs, as summarized as follows. To further improve the structural quality of the InAs/GaSb SLs, we employed GaSb as the substrate for the SL growth although the GaSb substrate has strong absorption in the mid-IR spectral region, which means that only front-side illuminating detector geometry is possible. First, GaSb buffer layer on GaSb substrates was optimized and then the growth condition for SL structure was studied. After the optimization of the growth for the InAs/GaSb SL, 100-period T2SLP structure (Fig. 10) was grown and the structure was characterized by structural and optical characterization techniques. For 100-period SL structures, microscopic cross-hatch and threading dislocation generation in the SL were observed from AFM and TEM due to the relaxation of strain accumulated from InAs mismatch.

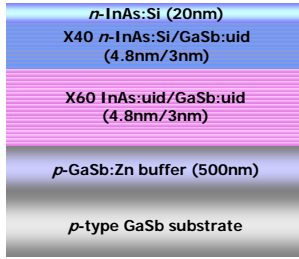


Fig. 10: Structure of T2SLPs on GaSb.

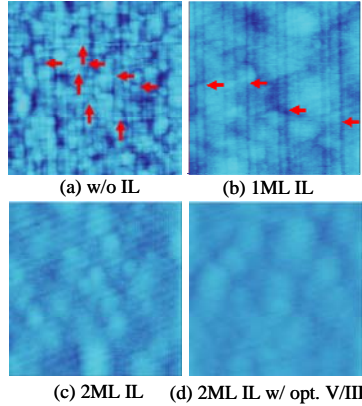


Fig. 11: AFM image of SLs with and without interlayer (IL).

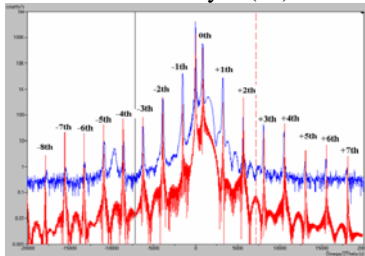


Fig. 12: (004) X-ray ω -2 θ scan of T2SLP with IL.

detector measured at 81K has cutoff frequency, $\lambda_c \sim 9 \mu\text{m}$, which is close to the SL design ($\sim 10 \mu\text{m}$).

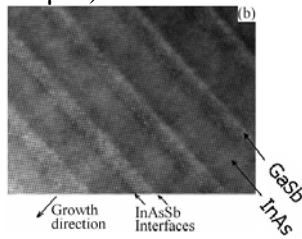


Fig. 13: TEM of T2SLP with IL.

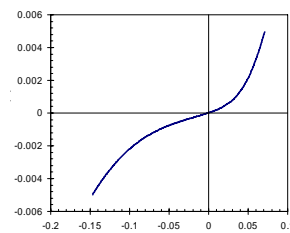


Fig. 14: I - V characteristic of T2SLP

In the case of MBE growth of T2SLP structures, introducing an interface InSb layer to counter-balances the tensile strain in InAs layer improved the structural quality of the SL. Unlike the MBE growth, our results show that, in the MOCVD growth of InAs/GaSb SL, introducing interface InSb layers deteriorates the quality of grown structures seriously and the InSb is the source of nanopipes. Since the optimized growth temperature for InAsSb can be higher than that of InSb (depends on the As composition in the alloy), we introduced $\text{InAs}_{0.8}\text{Sb}_{0.2}$ at the interfaces to compensate the tensile strain which is created by the InAs layer in the SLs. 2-ML interface layer (IL) of $\text{InAs}_{0.8}\text{Sb}_{0.2}$ with optimized V/III ratio resulted in cross-hatch-free surface with RMS surface roughness of 0.53nm and 0.23 nm for 20×20 and $5 \times 5 \mu\text{m}^2$ scans, respectively (Fig. 11 shows AFM image change indicating morphology improvement with increasing IL thickness from 0 to 2 MLs). The (004) XRD ω -2 θ scan (Fig. 12) of the InAs/GaSb SLs with $\text{InAs}_{0.8}\text{Sb}_{0.2}$ IL shows stronger intensity of 0th-order and higher-order of satellite peaks with narrower linewidth than one without IL, indicating improved overall material and interface quality of the SL structure by introducing IL. Improved interface quality of SL structure with IL was also verified by TEM investigation (Fig. 13). PL spectrum and absorption coefficient curve T2SLP on GaSb substrate show PL peak at $7.5 \mu\text{m}$ and well-matched absorption curve with one modeled by $8 \times 8 k \cdot p$ method. T2SLP epitaxial structure was fabricated into n - i - p mesa structure. Electrical and optical characteristics of the T2SLP were performed.

Dynamic impedance product area of the diode measured at 81 K, $R_0A \sim 0.0608 \Omega\text{cm}^2$ (Fig. 14). Photoresponsivity of the

In summary, Dupuis' group demonstrated InAs/GaSb type-II SL photodetectors grown by MOCVD operating at longer than $9 \mu\text{m}$. The performance characteristics can be further improved by further material quality improvement and controlling the p - and n -type doping, and the unintentional doping levels in the detector structures.

Summary of MURI Program Impact on Dupuis' Group Research

MURI program research summary

InP Quantum Dot Intersubband Photodetectors (QDIPs)

- Development of InP QD size, density, and spatial distribution control by altering growth parameters for SAQD growth

- Development of InP QD density and spatial distribution control by controlling nucleation for SAQD growth via matrix material control
- Development of vertically aligned size-controlled multiple stacking of InP QDs
- Strain management of multiple stacking of InP QDs by introducing AlGaP thin layer

Type II Superlattice Photodetectors (T2SLPs)

- Development of GaSb metamorphic layer growth on GaAs substrates
- Development of MOCVD growth technology for InAs, GaSb, InAs/GaSb SL
- Development of MOCVD-friendly strain balance layer for SL
- Demonstration of photo absorption and detectors on both GaAs and GaSb substrates grown by MOCVD
- Demonstration of photodetectors on GaSb substrates grown by MOCVD operating in mid-IR spectral region (longer than 9 μm)

Task 3: Quantum-Dot Infrared Photodetectors

Principle Investigator: K. Y. Cheng, Dept. of ECE, UIUC
 Graduate Student: Z. Zhang

Scientific Progress and Accomplishments:

This project thoroughly studied the design, characterization, and molecular beam epitaxy (MBE) growth of multilayer InAs QDs grown on InP substrate for the fabrication of quantum-dot infrared photodetectors (QDIPs). The key accomplishments of achieving efficient InAs QD QDIPs on InAlGaAs matrix layer lattice matched to InP substrate are summarized as follows:

(a) InAs QD formation mechanisms on InP-based materials:

To realize this goal, achieving single layer QDs with high morphological and optical quality is the foremost objective of this study. The evolution of the surface morphology of InAs nanostructures grown on InGaAs/InP by molecular beam epitaxy was studied through atomic force microscopy (AFM) imaging. Randomly distributed quantum dots and quantum wires were reproducibly achieved by adjusting proper growth parameters such as InAs deposition thickness, growth temperature, arsenic overpressure, and InAs growth rate. It is observed that a thick InAs layer (≥ 9 monolayers, MLs), high growth temperature, high arsenic overpressure, and high growth rate promote the formation of quantum dots. (Fig. 15) We propose that when InAs is deposited, the interaction of the total strain in the InAs layer and the surface strain distribution in the underlying matrix layer is the determinant factor of the nanostructure morphology. Thick InAs, which increases the total strain of the InAs layer, is preferred to form quantum dots. Surface diffusion of In adatoms is another important factor affecting the surface morphology. A high growth temperature promotes homogeneous diffusion, while high arsenic overpressure and growth rate reduces the surface diffusion of the In adatoms. These factors induce the formation of quantum dots.

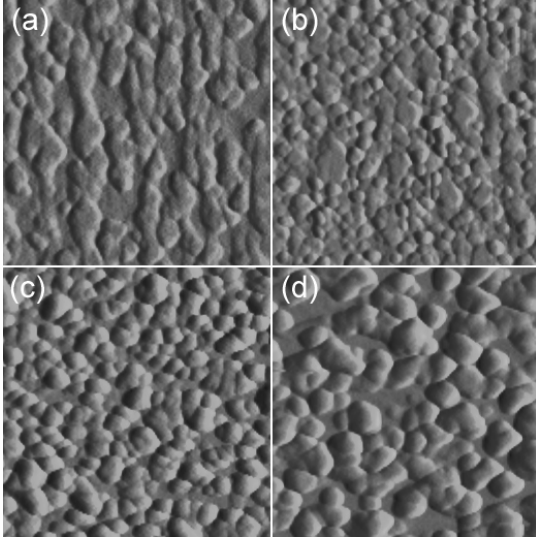


Fig. 15. AFM images of InAs nanostructures as a function of the InAs thickness. The equivalent InAs thickness was (a) 4 ML, (b) 6 ML, (c) 9 ML, and (d) 12 ML. The growth temperature was 500 °C. The arsenic overpressure was 5.3×10^{-6} torr and the growth rate was 1 ML/s. The size of the images is $1 \mu\text{m} \times 1 \mu\text{m}$ with the vertical axis aligned along [110]

(b) InAs QD formation on surface structure modified InGaAs superlattice:

We have developed a novel matrix layer structure, the InGaAs surface structure modified superlattice to suppress quantum wire formation, thus achieved high quality InAs quantum dots on (100) InP substrates. Formed by periodically repeating the group III- and group V-stabilized InGaAs layers, the InGaAs surface structure modified superlattice offers much greater advantages than the conventional InGaAs matrix layer for the growth of InAs quantum dots, where a thick InAs layer is required for the dot formation. (Fig. 16) By adjusting the number of period and the layer thickness of the superlattice structure, uniform InAs quantum dots are achieved even using an InAs deposition as thin as 2.5 monolayers. (Fig. 17) Photoluminescence (PL) measurements further verify a uniform size distribution of the achieved quantum dots.

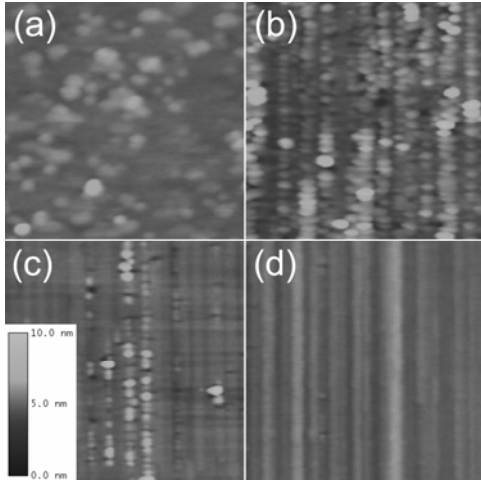


Fig. 16. AFM images of InGaAs surface structure modified superlattice as a function of the superlattice period: (a) 1-period, (b) 3-period, (c) 5-period, and (d) 7-period. The thickness of each layer in the superlattice was 20 Å. The size of the images is $1 \mu\text{m} \times 1 \mu\text{m}$ with the vertical axis aligned along the [110] direction.

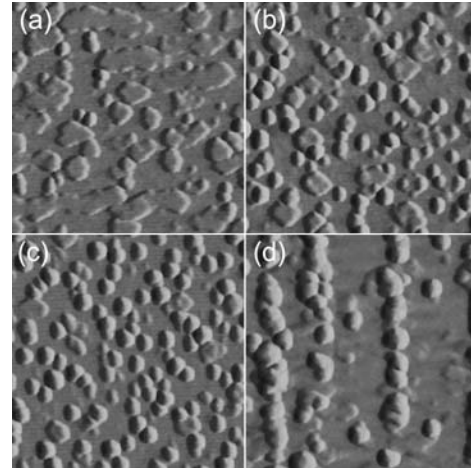


Fig. 17. AFM images of the InAs nanostructures grown on the InGaAs surface structure modified superlattice as a function of the superlattice period: (a) 1-period, (b) 3-period, (c) 5-period, and (d) 7-period. The thickness of each layer in the superlattice was 20 Å. The size of the images is $1 \mu\text{m} \times 1 \mu\text{m}$ with the vertical axis aligned along the [110] direction.

(c) QD surface morphology improvement

Although a high quality single QD layer has been achieved, stacking them into multi-layer structure still remains problematic. This is caused by the formation of 3-dimensional (3-D) growth front above the QD layer. Since QDIP structure usually requires stacking a large number of QD layers (>10) to improve the responsivity, the growth front becomes severely corrugated in the later QD layers. This leads to a non-planar interface between neighboring layers, which degrade the structural and optical properties of the structure. In order to solve this problem, two approaches have been developed in this project. In the first technique, a thin AlInGaAs barrier layer grown under a group III-stabilized condition is used to smooth out the 3-D growth front above the QD layer. The formation of the flat morphology is an act of balance between the surface migration of adatoms during the group III-stabilized growth and the strain field caused by the underneath QDs. The strain field in the InAs/InGaAs QD system promotes the formation of QDs along the $[\bar{1}10]$ direction. This strain field also affects the growth of the barrier AlGaInAs layer, making the growth preferably aligned along the $[\bar{1}10]$ direction. Meanwhile, in the group III-stabilized growth, the surface migration of group-III adatoms is preferred along the $[110]$ direction. The balance of these two effects can smooth out the 3-dimensional growth front uniformly and effectively, resulting in a flat surface as shown in Fig. 18.

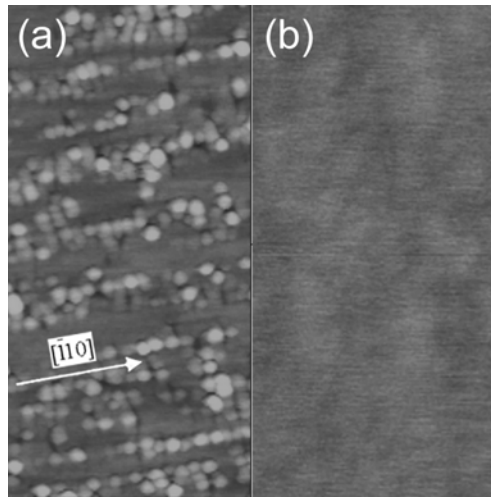


Fig. 18. The AFM surface images of QD samples covered by a 40 Å AlGaInAs: (a) the AlGaInAs was grown under a group V-stabilized condition; (b) the AlGaInAs was grown under a group III-stabilized condition. The image was $2\mu\text{m} \times 2\mu\text{m}$.

Secondly, a strain-balanced QD structure has been developed to solve the strain accumulation problem in fabricating high performance multilayer QDIP structures. The overall compressive strain caused by the formation of InAs QDs on InAlGaAs/InP is successfully balanced by inserting tensile-strained InGaAs strain balanced layers (SBL) immediately above QD layers. (Fig. 19) The overall strain effect of InAs QD (5 MLs thick) samples covered by SBL was characterized using high-resolution x-ray diffraction (HRXRD). Figure 20 shows the diffraction rocking-curves of 5-period InAs QD samples with 3.5 MLs, 5.5 MLs, and 7.5 MLs of InGaAs SBL. The highest intensity peak at 0° in all curves is from the InP substrate. The satellite peaks are distributed mainly on the left-hand side of the InP substrate peak, indicating a net compressive strain existing in the QD structure without SBL. When increasing the thickness of the InGaAs SBL from 0 to 5.5

MLs, the rocking-curve becomes more symmetric, indicating the overall compressive strain caused by InAs QDs is effectively balanced by the tensile-strained InGaAs SBL. When the thickness of the InGaAs SBL further increases to 7.5 MLs, the asymmetry in the diffraction rocking-curve shifts to the right-hand side of the substrate peak, indicating the structure is now under a tensile strain. These measurement results demonstrate that the overall strain in QD samples can be effectively controlled and engineered through the change of the SBL thickness, which provides a feasible way to optimize the device performance.

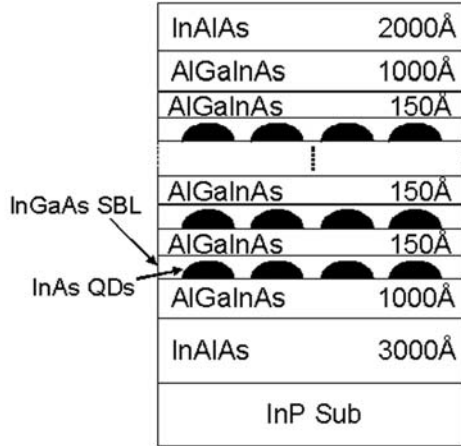


Fig. 19. Schematic of the strain-balanced InAs QD structure grown on InAlGaAs/InP. The 150 Å InAlGaAs barrier layer, InGaAs SBL, and the InAs QD layer are repeated to form the multilayer QD structure.

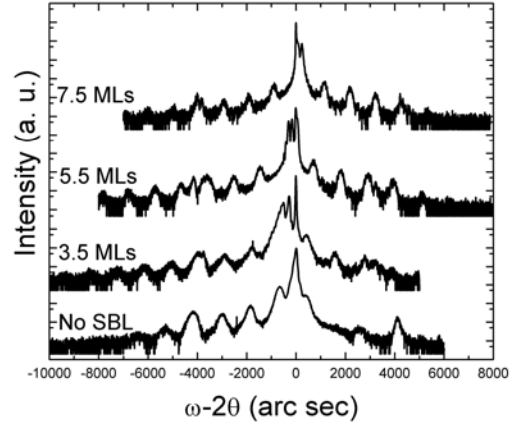


Fig. 20. HRXRD rocking-curves of 5-period InAs QD samples with different InGaAs SBL thicknesses. The peak with the highest intensity at 0° is from the InP substrate.

(d) Demonstration of defect-free 100-period InAs QD structure

The strain-balanced QD structure allows stacking a large number of defect-free QD layers for increasing the size uniformity of QDs as well as the optical absorption, which are essential to the high performance photodetector. As the first step toward the demonstration of a high-performance photodetector, a 100-layer strain-balanced InAs QD structure was grown.

As shown in Fig. 21, no visible defect was detected from the cross-sectional transmission electron microscopy (XTEM) measurements. A lower magnification TEM picture of the center 75 QD layers of the active region is shown in Fig. 21(a). Figure 21(b) shows the zoom-in image of the top 5 QD layers, indicating a defect free multilayer QD structure with smooth interfaces between neighboring QD layers even at top QD layers. Figures 21(c) shows the detail image of the strain-balanced QD layers. The QD nanostructures have an average base diameter of around 200 Å and height of 20 Å, which are consistent with the atomic force microscopy results of QD samples without cap layer grown under a similar condition. Furthermore, Figs. 21(b) and (c) also display a uniform QD size distribution in each QD layer and defect-free flat interfaces between QD layers.

The optical quality of the 100-layer QD sample was compared with several QD samples with identical structure but containing less (1, 5, 10 and 30) QD layers in the active region. As shown in Fig. 22, the increasing number of QD layers in the active region leads to

higher photoluminescence (PL) intensities at both room temperature and 77 K. This indicates the structural quality of QD samples does not degrade with more QD layers stacked in the active region. Besides, the strong room temperature PL intensity of the 100-layer QD sample proves that a low defect density in the structure has been achieved.

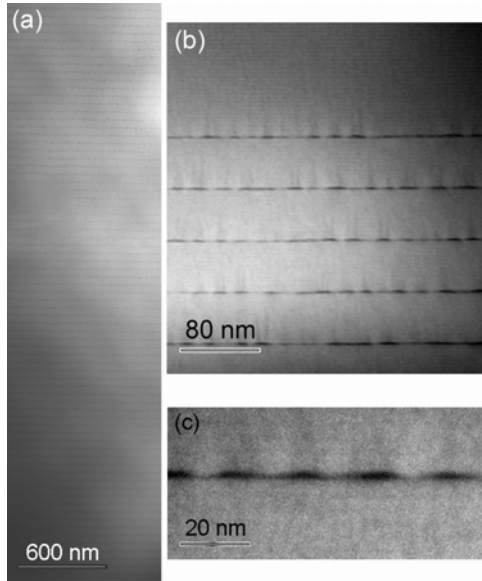


Fig. 21. XTEM micrographs of the 100-layer QD sample. (a) The center 75 QD layers. (b) The top 5 QD layers. (c) Zoom-in images of QD layers.

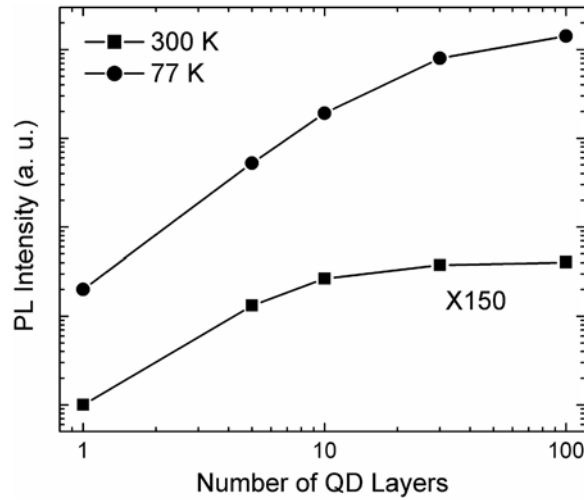


Fig. 22. Comparison of room temperature and 77 K PL intensities among QD samples containing various number of QD layers.

(e) Demonstration of InAs QD/InAlGaAs QDIPs grown on InP substrates

Based on the developed QD growth techniques, photoconductive-type InAs/InAlGaAs/InP QDIPs grown on InP by MBE technique were fabricated and tested. These devices demonstrated responses to normal incident photoexcitations in the 5-18 μm range. The QDIP device based on bound-to-bound transitions shows a peak responsivity of 113 mA/W and a detectivity of $1.8 \times 10^9 \text{ cmHz}^{1/2}/\text{W}$ at 10 K for a 10-period QD heterostructure. The device based on bound-to-continuum transitions demonstrates an improved dark current characteristics and a better detectivity of $2.1 \times 10^9 \text{ cmHz}^{1/2}/\text{W}$ at a peak wavelength of 7.5 μm . To the best of our knowledge, this is the first InAs QD/InAlGaAs/InP QDIP ever reported.

QDIP structures were grown by MBE on sulfur-doped (100) InP substrates. Figure 23 shows the layer structure of the device. The active region of the device contained 10-period InAs QD layers separated by 500 \AA InAlGaAs barrier layers. The nominal InAs layer thickness in each QD layer was 5 monolayers (MLs). Each QD layer was δ -doped using silicon to an equivalent 3-D electron concentration of $1 \times 10^{18} \text{ cm}^{-3}$, which corresponds to about 2 electrons per dot. The nominal dot density was $5 \times 10^{10} \text{ cm}^{-2}$. The active region of the device was sandwiched by InAlGaAs layers to ensure a symmetric structure. Figure 24 shows the responsivity spectra of the QDIP. The dominant absorption peak in the responsivity spectra is centered at 7.5 μm with a spectral width of 2 μm ($\Delta\lambda/\lambda = 27\%$). Another absorption peak centered about 18 μm can also be observed. The absorption peaked at 7.5 μm is due to the bound-to-continuum transition while the absorption centered

about $18\mu\text{m}$ is attributed to the bound-to-bound transition. Also shown in Fig. 24 is that a higher bias voltage increases the responsivity of absorption centered at $7.5\mu\text{m}$ apparently. The responsivity intensity at $18\mu\text{m}$ remains unchanged with increasing the bias voltage, indicating that the bound-to-continuum transition dominates the device operation. The evolution of the responsivity with absorption centered at $7.5\mu\text{m}$ as a function of the bias voltage is shown in Fig. 25. The responsivity increases linearly with bias up to 0.7V and increases much faster above 0.7V . The peak responsivity intensity was achieved under a bias voltage of 1.4V . Further increasing bias voltage leads to noisy signals due to the large dark current. Figure 26 shows the detectivity of the QDIP at various bias voltages. After the initial gradual increase, peak detectivity of $2.1 \times 10^9 \text{ cmHz}^{1/2}/\text{W}$ was achieved at a bias voltage of 0.8V . The detectivity then falls off with increasing bias due to the increased dark current.

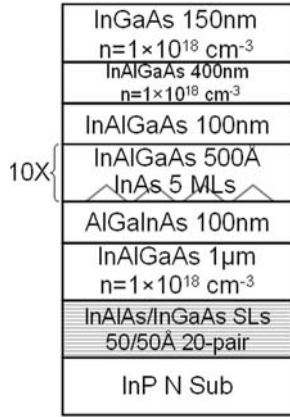


Fig. 23. Schematics of the QDIP structures.

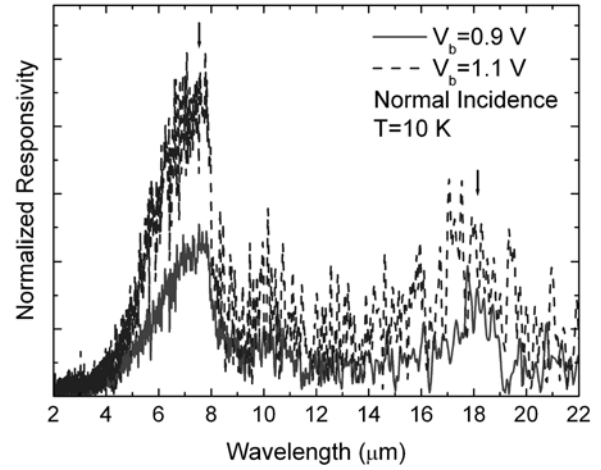


Fig. 24. Responsivity spectra of the QDIP measured under different bias voltages at 10 K .

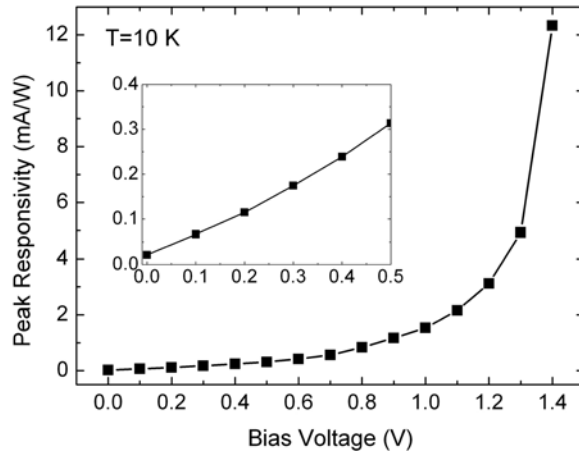


Fig. 25. Peak responsivity of the QDIP measured at varying bias voltages at 10 K .

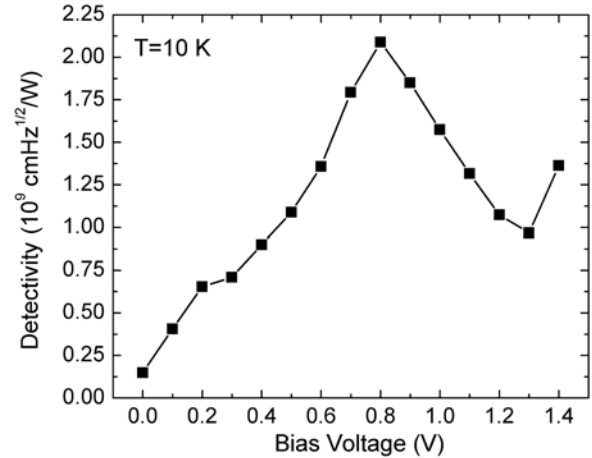


Fig. 26. Detectivity of the QDIP measured at varying bias voltages at 10 K .